nature communications

Article

https://doi.org/10.1038/s41467-025-65824-7

Bridging the gap between subduction dynamics and the long-term strength of the Sunda megathrust

Received: 19 September 2024

Accepted: 23 October 2025

Published online: 28 November 2025

Check for updates

Fabio A. Capitanio[1] ✉, Thyagarajulu Gollapalli[1,2,3], Radhakrishna Munukutla[2], Juan Carlos Graciosa[1,4], Zuhair Mohd[1,5], Adam Beall[1] & Luca Dal Zilio[5]

The link between great earthquakes and subduction dynamics across a wide range of scales remains a crucial, yet elusive, tenet of the seismotectonics of convergent margins. Here, we show high-performance computational simulations of the three-dimensional Sunda subduction zone dynamics matching plate motions, tectonics and current deformation, thereby providing insights into the stress regime of the Java-Sumatra-Andaman margin. Testing various tectonic forces reveals the primary control of the Java slab pull and induced mantle flow on the whole margin tectonics, driving northward-increasing oblique convergence, Sumatran trench advance and increased tectonic coupling along this segment. The modelled deviatoric stresses reproduce the geodetically-constrained interseismic compression in Sumatra and megathrust stress orientations notably consistent with the seismic P-axes, with magnitude comparable to static stresses on seismogenic faults. We map the frictional strength along the Sumatra-Andaman megathrust, identifying critical thresholds at key seismogenic depths, which remarkably correlate with the location of great earthquakes. Our outcomes show how subduction dynamics may critically prime the conditions for seismicity along the Sunda margin.

The most devastating seismic events, classified as great earthquakes ($M_w \geq 8.0$), occur along the plate interface of subduction zones, called the megathrust[1]. These earthquakes are explained within the framework of the subduction paradigm, which provides a context for stress distributions across scales, from the long-term tectonic loading over millions of years to the short-term stress released during seismic ruptures and its subsequent relaxation over years[2]. Although interconnected, these processes operate across vastly different spatio-temporal scales, making it a significant challenge for the scientific community, and society at large, to bridge our understanding across scales effectively.

The connection between subduction zones dynamics and their seismicity is exemplified by the megathrust strength, that is, the resistance of megathrusts to the action of tectonic stresses. The strength is the balance between the applied lithostatic and tectonic stresses, due to the mass distribution and the subducting slab-mantle interactions, and the intrinsic properties of the megathrust interface, due to fluids, temperature, lithology, and fault geometry, resisting (balancing) the applied stress. Constraining the strength of megathrusts requires integrating tectonics, structural features, geodetic and seismic strain across disparate scales. Geodetic imaging of the seismic and aseismic strain at major convergent zones shows that the

[1]School of Earth, Atmosphere & Environment, Monash University, Clayton, VIC, Australia. [2]Department of Earth Sciences, Indian Institute of Technology Bombay, Mumbai, India. [3]IITB-Monash Research Academy, Indian Institute of Technology Bombay, Mumbai, India. [4]Research School of Earth Sciences, Australian National University, Canberra, ACT, Australia. [5]Earth Observatory of Singapore, Nanyang Technological University, Singapore, Singapore. ✉e-mail: fabio.capitanio@monash.edu

strain accrued during the seismic and postseismic periods aligns with that accumulated between major earthquakes[2], showing that the viscous behaviour of the lithosphere-mantle system controls the strain across timescales[3], once the transient deformation due to earthquakes is relaxed. Therefore, several works have tested the controls subduction dynamics have on megathrusts seismicity, addressed within the context of tectonic coupling[4], i.e., the tectonic stress across the plate interface. Statistical analyses have highlighted correlations between seismicity and slab age, that is, their inferred buoyancy[5], upper plate strain[6], a proxy for tectonic coupling, and mantle tractions that may enhance interface stress[7]. Similar analyses also propose the statistical relevance of physical properties of megathrusts acquired during subduction, such as low megathrust curvature[8], increased roughness[9] and thick sediment accumulation[10]. These works reveal the key role of the balance between boundary stresses acting on megathrusts and the internal stresses, although constraining these processes beyond statistical correlations has been proven difficult.

Additional constraints are provided by tests of plate kinematics and static force balance, although these do not necessarily constrain the tectonic stress acting on megathrusts. The plate kinematics frame characterising the seismic coupling does not describe the stress in the interseismic period, when this can be nonuniquely associated with either vanishing stresses or high megathrust strength[4]. This frame has been called into question, with long-held views on plate motions-age relations confuted by recent seismicity[11] and the controversial potential to lead to unrealistic high seismic coupling estimates[12]. Megathrust stresses and tectonic coupling, have been addressed directly, from static force balance calculations[13] and its extension across stages of the seismic cycles[14], and from thermal and mechanical properties constrained by heat flow[15] and focal mechanisms[16] at subduction zones. These processes are different and occur at different stages of the seismic cycle and, although providing useful insights, they do not support a unified physical model for the stress loading and release at subduction zones[17].

The Sunda subduction zone serves as a pivotal case in seismotectonics, highlighting the challenges in understanding the complex interplay between subduction dynamics, long-term tectonics, and seismicity. This active convergent margin exhibits deformation consistent over the geological and seismic timescales[18], making it a valuable case for the test proposed here. The Sunda margin, between the Indo-Australian and Eurasian plates, comprises three major segments, namely, from north to south, Andaman, Sumatra, Java and Banda. The largest seismic energy has been released along the Sumatran segment, which hosted three great earthquakes of magnitude $M_w \geq 8.5$ within three years, among others and has highest coseismic strain of the region[19]. Notably, the 2004 Mw 9.3 Sumatra earthquake triggered a massive rupture stretching roughly 1300 km[1,20], from northern Sumatra to the Andaman Islands (Fig. 1a), the longest along this margin[21] (Fig. 1b). The estimated seismic coupling coefficient, i.e., the ratio between seismic and tectonic strain, in this area is close to unity[22], suggesting that the deformation integrated over the historical catalogue and that due to convergence must be comparable. The compatibility between short- to long-term deformation is shown by the relative thickening of the Sumatran back arc, ongoing since ~15 Ma[18], the advancing motions of this trench (Fig. 1a, red arrows), as opposed to the retreat in the other segments[23], and matching GPS-constrained interseismic contraction in Sumatra[19], that is, net of transients due to large earthquakes. Further evidence of this regime comes from flexural[24] and seismotectonics analysis[25] along the Sumatran segment, illustrating near-trench compression in the downgoing plate, extending this regime across the margin. The deformation accrued over million years and that constrained geodetically, shows that the strain pattern is consistent across time scales, with the largest compression localised in the Sumatran segment, while further away from the trench, part of the deformation is accommodated by transcurrent faulting[21,26].

The deformation along the Sunda margin squarely challenges the subduction paradigm. The direction of plate motions in this area varies progressively northward, from trench-perpendicular to nearly trench-parallel (Fig. 1a). This implies that the fastest convergence is along Java and the slowest along Andaman, which is at odds with the deformation distribution along the margin, with major compression and strike-slip in Sumatra and Andaman, respectively, where lower convergence does not reconcile with intense tectonics. How this can be explained by the subduction paradigm remains unclear: the strongest earthquakes and compressional tectonics are located where the subduction forces are inferred to be the weakest, challenging the idea of driving slab pull forces. Beneath central Sumatra, the upper mantle slab shallows up abruptly from >600 km deep, beneath Java, to only ~300 to ~400 km, then becoming <200 km deep beneath Andaman[27–29]. The age of the subducting lithosphere near Sumatra is the youngest, ~46 Ma, making it the thinnest, and the slab has the shallowest dip (Fig. 1a, b), while in Java it is ~150 Ma, and ~100 Ma in Andaman. For such a short, thin slab the lowest slab pull and ridge push forces[18,30] may be invoked, and yet this is where most intense seismic and tectonic activities occur. Additionally, the slab has a step beneath Sumatra, and an older and thicker slab is found beneath Java (Fig. 1a), reaching ~600 km depths, extending further east to the Banda Sea, where subduction is disrupted by the arrival of the continental Australian lithosphere[31]. Yet, the stronger slab pull expected from the Java slab is associated with reduced great earthquakes occurrences, that is, seismic energy release, and tectonic shortening. This enigmatic association, also observed in other margins where similar slab steps are present[32], warrants further investigation.

Here, we propose a computational approach to characterising the stress and strain at the Sunda convergent margin and plate interface, the megathrust, as a result of the subduction force balance, providing insights into the seismotectonics of this area. We set up a numerical model of the Asian margin, from the Indian collision to the Sunda subduction zone, assimilating geophysical and geological observations from the Indo-Australian and Asian plates and the upper and lower mantle structures, to reproduce realistic terms of the force balance (Fig. 1). This approach has been proven to reconcile subduction dynamics with self-consistent stress and strain distribution across scales[33], their relation with plate margin motions[34] and magnitude of earthquakes[35,36]. We devise different setups to systematically test different tectonic forces, from that of the Sunda slab to that of the Indian mid-oceanic ridge, and from the force of the Indian collision to that of the lower mantle mass and flow. Our approach is consistent with previous work focused on seismic energy and centroid moment tensors[37], plate motions and mantle flow[38,39] and is here extended to include a self-consistent plate interface constitutive behaviour, critical to the realistic simulation of stress at convergent zones[34,40]. The models are validated against observed plate motions, upper plate tectonics, geodetically-constrained strain rates and compressional (P) axes from earthquakes centroid moment tensors catalogue, proving the consistency of the computed stresses. We focus on the deviatoric stress components, that is, the stress magnitude at which creep or frictional sliding occurs (Methods section). This represents the stress that is eventually accommodated over the long-term, net of the seismic transient, and allows the discussion of the long-term stress on the Sunda megathrust. Our outcomes support the discussion of the conditions for rupture and seismicity of the southeast Asian margin, bridging the gap between subduction dynamics, seismotectonics and the strength of megathrusts.

Results

Modelling the geodynamics of the Sunda subduction zone

We provide a comprehensive test of how fundamental tectonic forces control margin stress and strain by solving the force balance of

https://doi.org/10.1038/s41467-025-65824-7

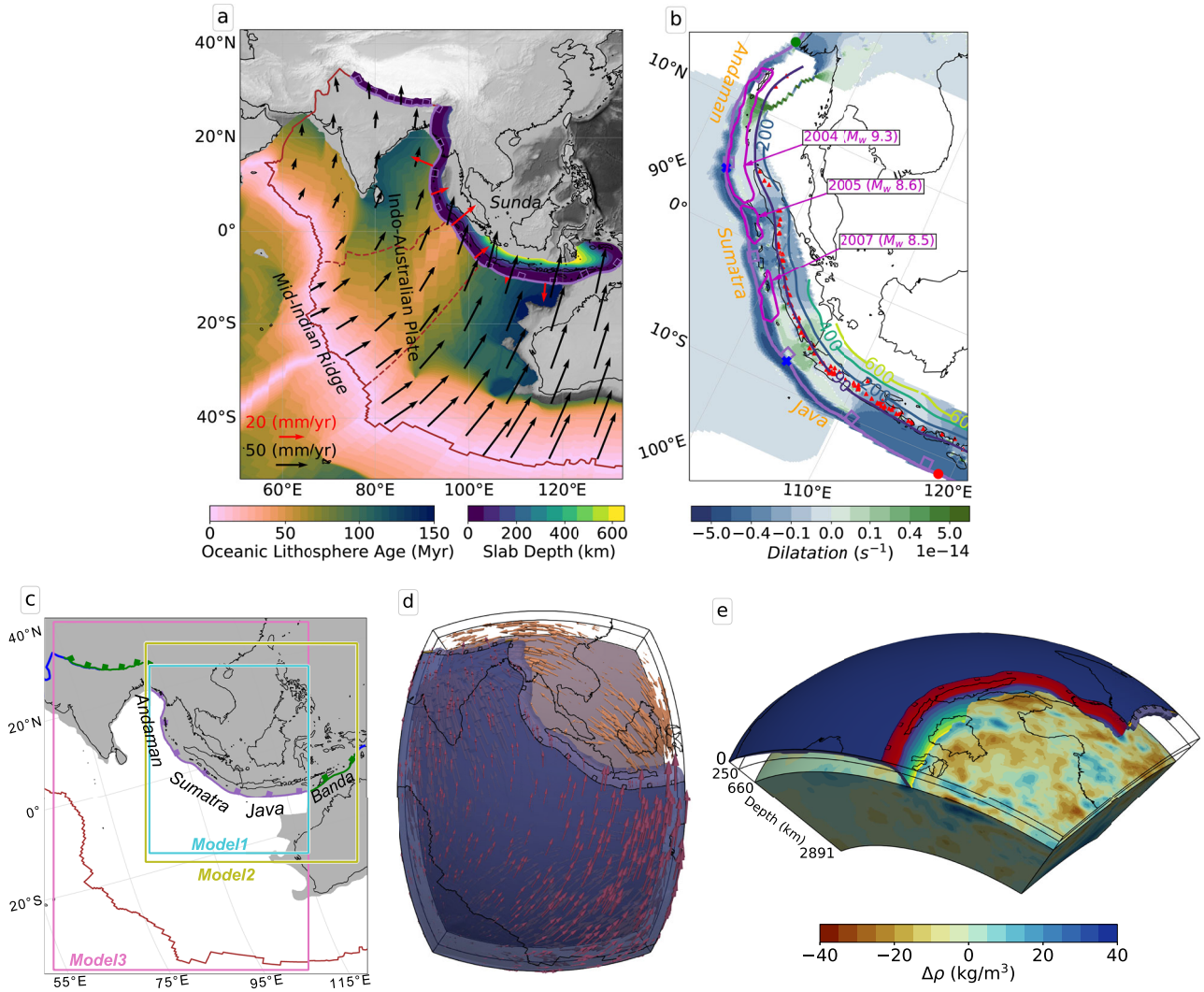

Fig. 1 | Sunda margin seismotectonics and numerical model. a Tectonic setting of the Southeast Asian subduction zone. Black arrows indicate the relative velocity of the Indo-Australian Plate (IAP) compared to the Sunda Plate in the No-Net-Rotation (NNR) reference frame[19]. Red arrows for trench velocities in the NNR frame[23]. The line with squares marks the Sunda trench location. Slab depth variations in the upper mantle is shown next to the trench[27]. Within the IAP, crustal ages are displayed in the oceanic region[41] along with topography variations in the continental area. The solid dark red line represents the boundary of the entire IAP. The dashed dark red line indicates the internal boundary separating the Indian, Capricorn, and Australian plates within the IAP. **b** Dilatation along the Sunda trench[19]. Positive and negative values represent extension and contraction, respectively. The Sunda trench is divided into Andaman, Sumatra, and Java segments along the margin. Volcanic islands in red triangles. Contours show rupture patches of 2004, 2005, and 2007 earthquakes (http://equake-rc.info/srcmod/). **c** Outline of the different models developed in this study. **d** Numerical solution for the velocities of the subducting plate (magenta) and mantle flow (orange). **e** Model 3a setup. In blue the subducting lithosphere, in red the interface (megathrust) to a depth of 90 km. Lower mantle tomography as in the text, converted in density contrast. **a**–**c** were created with open-source software Python and library Matplotlib, (**d**, **e**) with open-source software Paraview.

subduction, encompassing the whole mantle and plate interactions, through high-performance computational modelling.

The fundamental subduction force balance in this region arises from the negative buoyancy of the Indo-Australian slab in the upper mantle, its variation due to the strong depth and thickness gradient along the margin, the resistance of the viscous upper mantle and the interactions with the Sunda-Asian upper plate. These features are embedded in the reference Model 1 using the oceanic crust age[41] to infer age-dependent lithosphere thickness and ridge push (Fig. 1c), while the buoyancy of the continental lithosphere is reduced (see Methods). At depth, the slab thickness and extent in the upper mantle are reconstructed using the Slab2 dataset, embedding Benioff zone, seismic reflection and tomography data[27]. Including the southeast Asian margin only and a passive lower mantle from 660 to 1000 km depth (Fig. 1d and Supplementary Figs. S1 and S2) the Model 1 serves as a reference to assess the most fundamental force balance of slab pull and mantle tractions only and their gradients along the margin.

Additional forces, external to the subduction zone, may act on convergent margins altering the fundamental force balance. These far-field forces are the mid-Indian Ocean ridge push and the lower mantle drag, due to the sinking slab mass imaged by tomography in the region. The contribution of individual tectonic forces to the margin stresses are addressed by extending the modelling space to include different plate boundaries and mantle depths of the region in several setups (Fig. 1c). Model 2 extends to the east to the Banda Sea and tests the role of the subducting Australian continent increased buoyancy and mantle flow, other parameters are unchanged. Model 3 includes the whole tectonic plate from the Indian Ocean ridge to the India-Sunda trench, combining the full ridge push and Indian collisional forces with the pull of the southeast Asian and Indian slabs in the upper mantle. The boundaries between Indian, Capricorn and Australian

https://doi.org/10.1038/s41467-025-65824-7

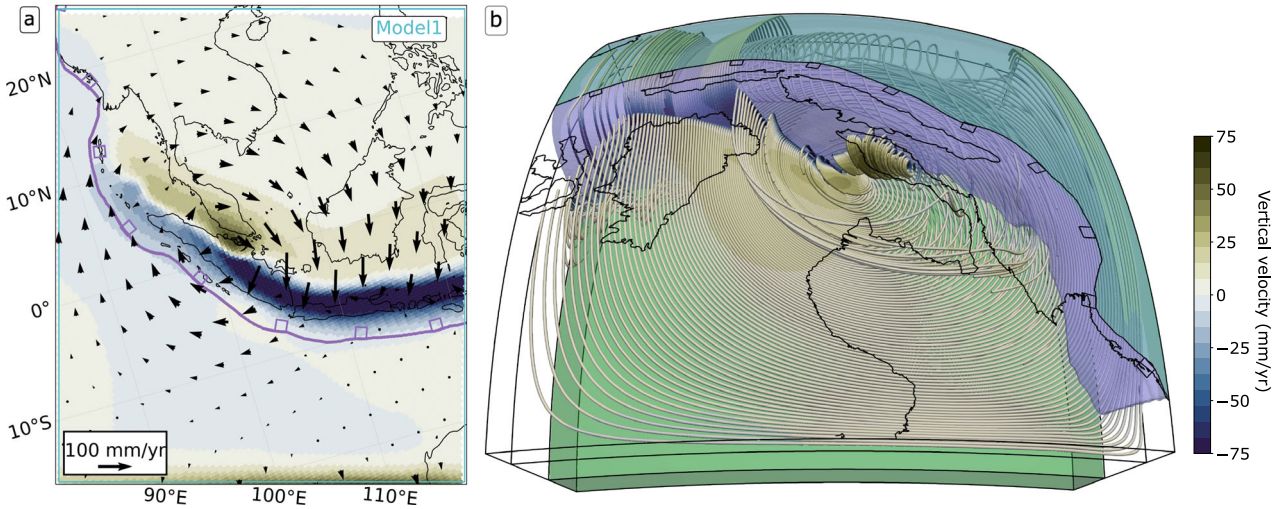

Fig. 2 | Modelled mantle flow beneath the Sunda margin. a Mantle flow at 300 km depth in Model 1. Arrows for horizontal flow velocities, in color for the vertical velocity. **b** Mantle flow streamlines, in color for the vertical velocity. Positive vertical velocities represent mantle upwelling, whereas negative vertical velocities indicate mantle downwelling. In dark green the subducting lithosphere and blue for the subducting slab. Lower mantle in light green. **a** was created with open-source software Python and library Matplotlib, **b** with open-source software Paraview.

plates are not implemented due to lack of observational constraints, although our lithosphere models embed the thinning of the lithosphere in the Capricorn zone, due to the varying oceanic crustal age (Fig. 1c and Supplementary Figs. S1 and S2). Model 3 extends to the core-mantle boundary, 2891 km deep, with a passive mantle in this setup, that is, has no density anomaly to drive flow, and extends to include the Indian continental and oceanic lithosphere, accounting for the Indian collision and ridge push force, respectively. In additional models, we vary the properties inside the Model 3 space and refer to these with a letter added to the numeral (3a to 3c, here). In these models we add the mass in the lower mantle, not included in the Slab 2 dataset, using tomographic P- and S-wave models, MITP08 and Smean[42,43], in Model 3a and 3b, respectively. These bracket end-members velocity anomaly distributions and smearing[44], whereas the tomography's anomalies in the upper mantle are neglected[38]. While different tomographic models exist, the models chosen have validated conversions to density contrast[45], which critically reduces the complexity of our modelling (see Methods). Model 3c is the same of Model 3a, but the density of the Himalayan slab is increased to match the excess inferred driving forces on the Indian plate[46] and lithosphere tractions arising from mantle flow[39]. We refer to these as active lower mantle models.

The modelled forces are balanced solving the conservation equations under the assumption of Stokes flow of an incompressible fluid, e.g., refs. 38,39. The force balance of the Stokes flow indicates that stress primarily depends on buoyancy contrasts, therefore gradients of stress along the margin are the result of the three-dimensional geometries and distribution of, most notably, slab mass in the mantle, while the material constitutive laws do not vary within the model space.

With the distribution of mass and the constitutive laws constrained, solving the conservation equations for Stokes flow yields self-consistent plate motions, mantle flow, and distributions of stress and strain rate (Fig. 1d). The models run for a small number of time steps, until subduction velocities reach stability, and we show results from a single time step, corresponding to a time of ~700 kyr. Under the assumption of the instantaneous solution, temperature variations due to advection and diffusion are neglected.

In our computational method, Lagrangian particles embedded in the finite element mesh improve the solution of the shearing along the margin, tracking accurately stress and deformation of different materials in the model domain. Additionally, a test of composite constitutive laws for the mantle shows that the stresses along the interplate margin, the focus of our work, are mainly dependent on plasticity, and less dependent on mantle creep. We have tested Newtonian and a range of non-Newtonian mantle creep laws (Methods), showing that the patterns of convergence velocities are mostly similar with all rheologies tested, while the magnitude varies only by a factor ~1.4 (Supplementary Fig. S3). Similarly, stress and strain rates around the plate margin keep consistent patterns, although the magnitude may vary up to a factor 4 and 10 for the stress and strain rates, respectively. The calculated values are compatible with the observables, although further constraining these values is limited by the uncertainties in the constitutive laws[47]. In the reminder of this work, we only show the results of Newtonian mantle models. This approach is commonly followed and capture the fundamental force balance involved[34,39,40,48], while minimising computational costs. Tests the free-slip top boundary condition against a pseudo-free surface[49], show negligible differences in our model set up (Supplementary Fig. S4). Also, varying the modelling space size imposes an inherent constrain on the large-scale mantle flow. However, this only alters the flow locally to the far walls and we show later that the impact on the flow around the slab is negligible.

Controls on strain and stress of the Sunda subduction zone

We present the six models described above to investigate on the role of the forces of subduction and mantle flow in the current deformation and tectonic coupling of the Sunda margin. Our results show that the models reproduce plate convergence, trench motions, and strain consistent with what observed along the Sunda margin. We show that the strain and stress fields at the subduction zone are primarily controlled by the attached slab mass distribution and the upper mantle flow, while lower mantle flow and far-field forces affect mostly plate motions and upper plate deformation patterns away from the trench.

We show in Fig. 2 the result of Model 1, where only the slab and upper mantle are modelled, and illustrate the complex flow arising from the gradients in slab depth, increasing the tractions beneath Sumatra. In the Java segment, the flow is coupled with the downgoing slab and it is mostly entirely poloidal. Instead, further north, the flow is complicated by the varying slab depth, and the mantle is forced around the slab edge, upwelling from the sub-slab to the mantle wedge region beneath central Sumatra (Fig. 2 a). This mantle flow pattern is

https://doi.org/10.1038/s41467-025-65824-7

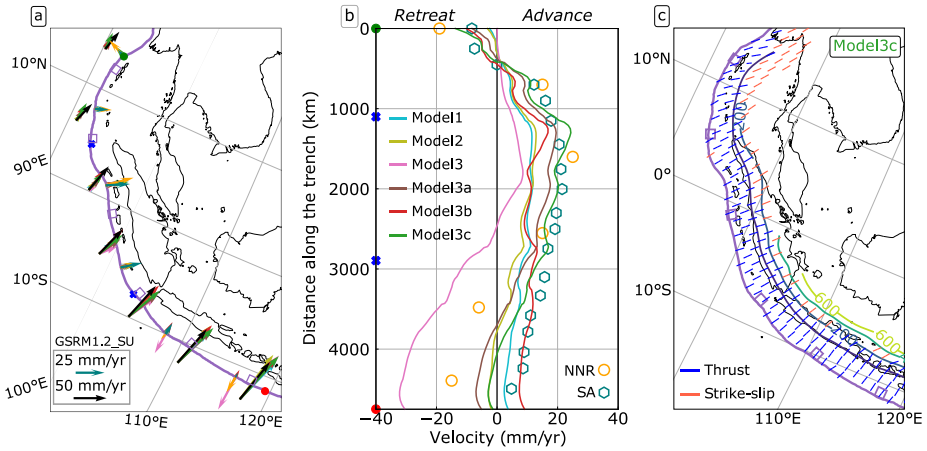

Fig. 3 | Plate motions, trench velocities and tectonic regime. a Modelled plate and trench motions and comparisons with the GSRM1.2 dataset using a Sunda-fixed reference frame, GSRM1.2_SU, and trench velocities from seafloor spreading-aligned[51] dataset, SA. Model legend in (**b**). **b** Modelled (solid lines) and observed trench motions in the seafloor spreading-aligned[51] reference frame (SA, hexagons) and No-Net Rotation (NNR, circles) reference frame[23]. **c** Tectonic regime defined by stress tensor. Major compressional eigenvector for thrusting (blue) and strike-slip (orange). All the panels were created with open-source software Python and library Matplotlib.

compatible with shear wave splitting and receiver functions analysis, showing the upwelling mantle from the Sumatran sub-slab to the mantle wedge[50]. We show that the escaping mantle from the Java sub-slab region result in the largest vertical velocity and, therefore, in excess trench-ward tractions beneath the Sumatran upper plate segment (Fig. 2b). Additional tests show that other forces, namely, continental subduction along the Banda segment and mantle flow around the slab (Model 2), ridge push and passive lower mantle (Model 3), and lower mantle slab mass and flow (Model 3a, b, c), do not alter the increased upwelling and tractions beneath Sumatra, and only affect the large-scale flow field, far from the margin (Supplementary Fig. S5).

A critical test of the models consists in the ability of the modelled subduction dynamics to reproduce realistic plate and trench motions. All models reproduce the characteristic northwards-increasing oblique convergence along the Sunda margin and oblique motions along the fore-arc[12] (Fig. 3a, Supplementary Fig. S8). The variable error is minimised in models with lower mantle mass, in different reference frames, with Model 3b and 3c best aligned with plate motions in the GSRM1.2_SU, that is Sunda-fixed reference frame (Supplementary Fig. S9), showing the anchoring effect of the sinking slabs in the lower mantle. The models' trench motions are compared to the observed trench velocities in the seafloor spreading-aligned[51] (SA) and in the No-Net Rotation[23] (NNR) reference frames, which bracket the end members proposed for realistic trench motions including and excluding net-rotation, respectively. The trench motions in both reference frames agree on the fastest advance of the northern Sumatra trench, up to ~25 mm yr^{-1}, progressively decreasing outward to trench retreat of −20 mm yr^{-1} in Andaman, whereas bracket Java trench motions between +18 and −18 mm yr^{-1} (Fig. 3b). This pattern is coherently reproduced by all models, although the magnitude varies. Java trench retreat velocities are compatible with all models', except Model 3, where the passive lower mantle likely enhances trench retreat. The modelled trench velocities align well with observed values in Andaman, whereas the best matching models for the Sumatran advance are those with an active lower mantle, constrained by tomography, Model 3a, b, c, while Models 1 and 2, reproduce the pattern but underestimate the trench advance by ~50%. Further constraining the magnitudes of the trench motions may be prevented by the modelling simplifications adopted. This is mostly due to the lack of a full torque around plates[52] and a global mantle flow[38], and the choice of boundary conditions.

The stress solutions in our models define regimes compatible with the Sunda margin tectonics (Fig. 3c). Although the upper plate rheology does not include plasticity, tectonic regimes can be defined by the stress tensor's eigenvectors in the absence of explicit faults, indicating thrusting regimes, under which reverse faulting occurs (blue), and transcurrent regime (orange), under which strike-slip faulting occurs. Our results reveal persistent thrusting in the forearc, a characteristic feature of subduction margins, in agreement with the observed thickened lithosphere and crust[18,53], geodetic strain[19] and thrusting in western Sumatra[54] and Java[55]. The region of transcurrent regime in our models extends from the Andaman back-arc to central Sumatra, in agreement with the extent of a major strike-slip fault system, which has been estimated to accommodate up to ~30% of the total deformation[21,26].

The strain rates in the upper plate along the subduction zone, further illustrate the first-order control of the deep Java slab on the increased tractions along the Sumatran segment. The interactions between the slab's negative buoyancy and upper mantle flow, only components of the force balance in Model 1 (Fig. 4a), explain the contraction along the trench and forearc, peaking at ~ -10^{-14} s^{-1} in the Java-southern Sumatra segment, decreasing further north. These strain rates follow the gradient in the slab mass along the margin, with largest slab pull in the south, where slab reaches ~600 km (Fig. 4a, labelled and colored contours). Contraction rapidly vanishes in the back-arc in the southern and northern domains of the convergent margin, however, the contraction remains strong in Sumatra, $O(-10^{-15}$ $s^{-1})$, extending to the downgoing plate, in the forebulge area. This further supports the role of far-field forces, that is, the additional pull of the neighbouring Java slab and the increased mantle tractions. Note that the choice of different mantle and upper plate creep laws may affect the magnitude of the strain rates, although do not alter their distribution.

Far-field forces have negligible impact on the strain patterns at the margin and only influence the upper plate strain far from the margin. Model 2 shows minor variations in strain rates in the Java back-arc compared to Model 1 (Fig. 4b), following the inclusion of the Banda arc slab segment and Australian continent subduction. Model 3 has a ridge push and a whole, yet passive, mantle, and shows similar strain pattern to Model 1, although the entire upper plate is under extension (Fig. 4c). This is reversed in Models 3a, 3b, and 3c where lower mantle density derived from seismic tomography drives active mantle flow, enhancing far-field trench-ward tractions (Fig. 4d-f). The MITP08 tomographic model in Model 3a results in the same overall pattern as Models 1 and 2, with values slightly higher in the back-arc and lower in the Indian ocean lithosphere (Fig. 4d). Similarly, the Smean model in Model 3b only

https://doi.org/10.1038/s41467-025-65824-7

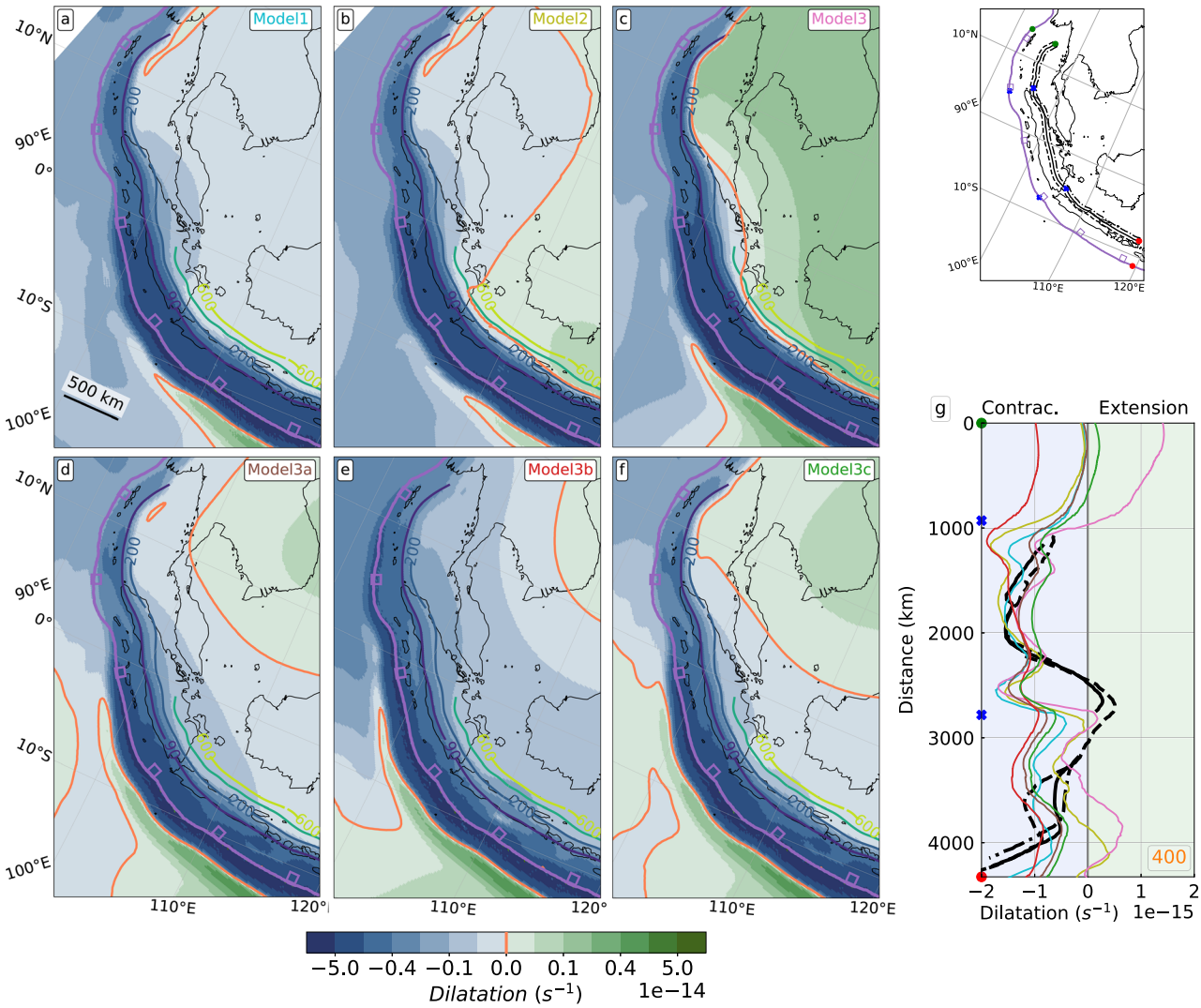

Fig. 4 | Modelled dilatation along the Sunda margin. a Model 1, upper mantle slab only, **b** Model 2, as in Model 1, slab extending to Banda, **c** Model 3, whole IAP and passive lower mantle, **d** Model 3a, as in Model 3, lower mantle densities as in Fig. 1c, **e** Model 3b, as in Model 3, lower mantle densities from Smean tomography (see text), **f** Model 3c, as in Model 3a, buoyancy of the Indian slab is increased. The magenta line with squares marks the location of the trench. Contour lines for the slab depth. Negative and positive dilatation in the upper plate indicate horizontal contractional (blue) and extensional (green) strain regimes, respectively, while the orange line is for 0 dilatation. **g** Modelled dilatation along a trench parallel profile in the back-arc region of the Sunda plate. Solid colored lines for the models (color-coded as in a to **f**). Dashed and dotted-dashed black lines show observed values from profiles at 400 ± 50 km due to discontinuities in the observation dataset. The inset map illustrates the location of the profiles. All the panels were created with open-source software Python and library Matplotlib.

induces increased contraction in the upper plate, far from the trench (Fig. 4e). Finally, the increased Indian slab pull in Model 3c does not reveal any significant difference (Fig. 4f). The strain pattern at the margin and the broad strain peak around Sumatra remains consistent in all models tested, as well as the extension in Andaman, except for Model 3b, while the deformation in the far-field in Java remains poorly constrained by observations.

The models' dilatation patterns reproduce the observations constrained by geodetic measurements along the Sunda margin[19], further attesting for consistency (Fig. 1b). The dilatation dataset excludes data from stations or periods affected by transient phenomena, reproducing the patterns that best represent the interseismic deformation[19], this is the background deformation over the whole catalogue periods, comparable to the tectonics[18]. Our analysis focuses on major areas where modelled rates agree with the observed dilatation (Supplementary Fig. S6), extending from the trench to the back-arc in north Sumatra and east Java, east of 110°E, and in small domains of the Andaman basin, while overestimated strain rates in the domains in between may be due to the incomplete nature of the data or to our simplified Sunda plate model. The dilatation patterns are comparable to the second invariant of the strain rates (Supplementary Fig. S7), providing a similar match to the observables. In a profile of the observed and modelled dilatation (Fig. 4g), we show dilatation rates of ~ -10^{-15} s^{-1} along a profile at 400 km from the trench, matching to the first-order the observations, with highest contraction in the Sumatra and Java. Model 2 and 3, which incorporate the Australian continent subduction along the Banda segment and the ridge and passive lower mantle, respectively, predict extension north-east of Java, suggesting these must enable trench migrations. Conversely, all models except Model 3a and b capture the Andaman back-arc extension. The area under extension remains rather small in the Models 1 and 2 and is more pronounced in Models 3 and 3c, where slab subduction and ridge push and lower mantle, respectively, are included. Our models accurately capture the pronounced extension observed between the compressional regions of the Sumatra and Java segments, although whether this reflects a tectonic feature remains speculative.

https://doi.org/10.1038/s41467-025-65824-7

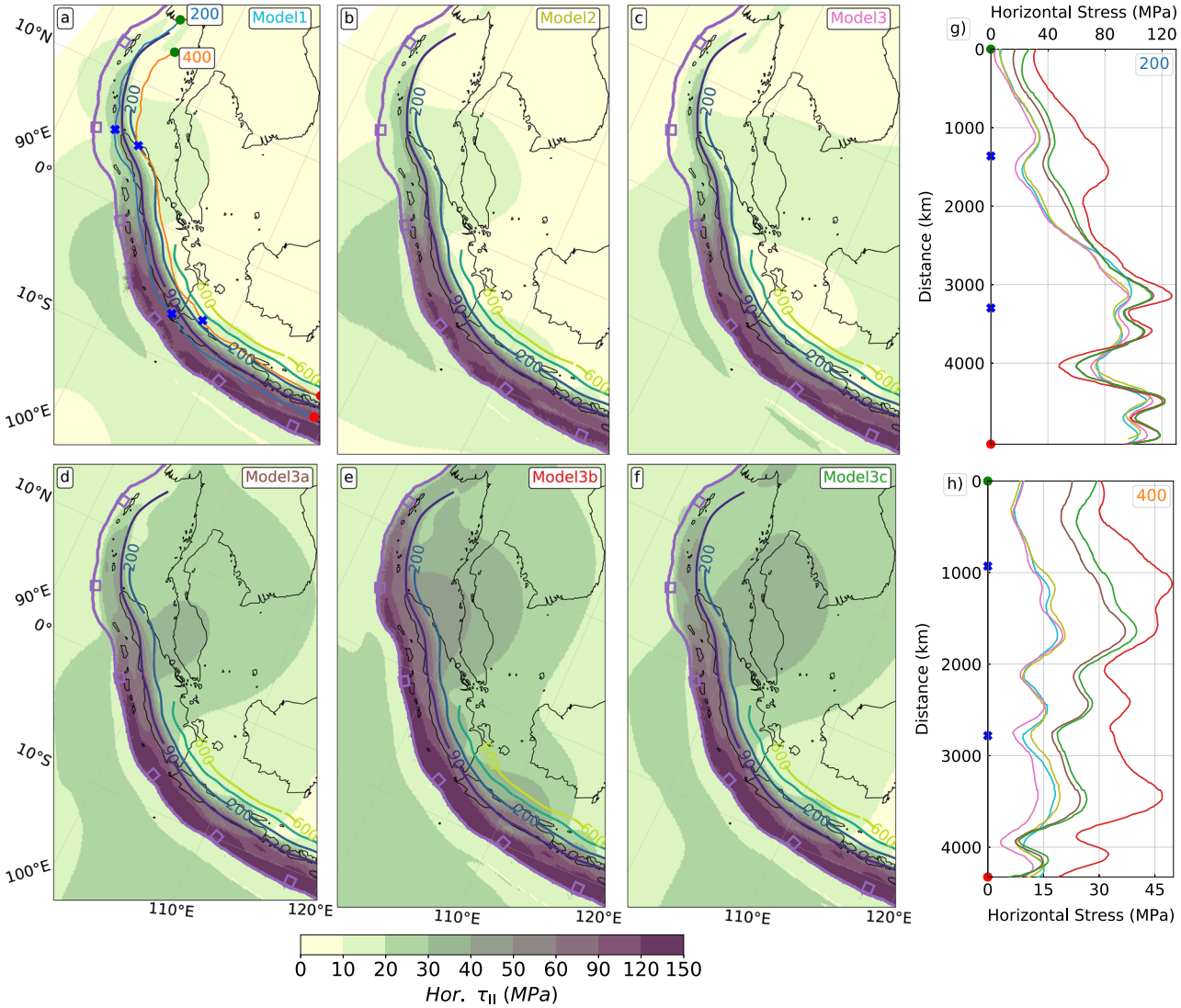

Fig. 5 | Modelled horizontal stress along the Sunda margin. a–f Stress invariant for models 1 to 3c, as in Fig. 4. **g** Model stresses in the arc, 200 km from the trench, and in the back-arc (**h**), 400 km from the trench, location in (**a**). The magenta line with squares marks the location of the trench. Contour lines represent variations in slab depth in the upper mantle. All the panels were created with open-source software Python and library Matplotlib.

The stress patterns at subduction zones further emphasise the primary control of the slab pull heterogeneities in the upper mantle, whereas additional far-field forces only impact the magnitude of the back-arc stresses. The horizontal stress invariant at the surface, τ_{II}, in all models shows high values of ~150 MPa in the Java and southern Sumatra forearc and decrease further north. In the back-arc, τ_{II} is relatively higher in the central Sumatra to Andaman compared to its southern parts (Fig. 5a-c). The addition of an active lower mantle, that is, when flow is sustained by the tomography-constrained densities, increases the τ_{II} magnitude in the back-arc (Fig. 5d-f), as shown by the increased compressional strain rates. The regional stress patterns show increased stress around Sumatra in both the overriding and downgoing plates. The arc profile shows high τ_{II} values of 100-120 MPa from Java to southern Sumatra, progressively decreasing northward to values < 40 MPa (Fig. 5g). The increased stress in the downgoing plate supports the role of Java slab pull forcing, through the rigid downgoing lithosphere, not easily explained by mantle tractions alone.

The higher τ_{II} in the Java to southern Sumatra forearc is almost independent of the far-field forces and the lower mantle mass, as all models follow the pattern of Model 1, with the slab only. Instead, the back-arc profiles, located 400 km from the trench (Fig. 5h), show lowered stresses, < 40 MPa, however, these are of comparable magnitude all along the margin, which is explained by the controls of the dynamics of the Java subduction in the upper mantle on the whole region, as shown for the strain rates. Additionally, the stress patterns are mostly similar, although the magnitude increases in Model 3a-c, revealing that the modelled lower mantle mass can increase the magnitude of the stresses, but has minor impact on their distribution, primarily set by the upper mantle slab buoyancy gradients.

Discussion

Reconciling plate boundaries deformation across different spatio-temporal scales has remained challenging, yet central to constraining subduction forces at shorter timescales, and to the seismic cycles of convergent margins. Our models support the idea that the stress along the convergent margins primarily depends on the slab mass and, most notably, its distribution along the trench. Most importantly, the outcomes highlight the role of slab steps, due to abrupt change in the slab depth, which leads to excess slab pull applied along the trench and increased tractions. We highlight the forcing on neighboring slab segments, acting as excess far-field forces, underscoring the

importance of considering convergent margin tectonics within a fully three-dimensional framework.

We show high compressional stresses and contraction in Sumatra extending over a broad area across the margin from the downgoing plate to the back arc. This regime is not explained by the force balance of the short Sumatra-Andaman slab subduction, and is instead, due to pull of the neighbouring Java slab and mantle flow around the slab step beneath Sumatra, locally increasing the stress between the plate, i.e., the tectonic coupling. This regime is compatible with observed thrust seismicity in the forebulge in this segment[25] and excess in-plane compression of the lithosphere of ~40 MPa, constrained by flexural[24] and buckling analysis[56], thin-shell intraplate stress modelling[57] and boundary forces scaling[48].

The slab step beneath central Sumatra, where the slab becomes abruptly shorter, critically emphasises the forcing of the neighbouring deep slab on the incoming plate and the enhanced mantle tractions, adding far-field forces to the Sumatran segment force balance, where the low pull of a too young and thin slab cannot drive the observed tectonics. This is the result of Model 1, where no other forces than upper mantle slab and flow are included, and remains unaltered by any other additional force modelled. The forcing of the Java subducting slab pull on the Sumatran segment is in agreement with what proposed previously[18], as the incoming lithosphere is partly accommodated at shallow depth, increasing the tectonic coupling[30]. The increased mantle tractions shown are in agreement with models of intraplate stresses, complementary to the approach followed here, and similarly emphasise the dominant role of mantle tractions around the whole margin[58], invoked to explain excess Sumatra boundary forces and deformation[25,48,57].

Alternative explanations for the increased tectonic coupling along Sumatra have been proposed, although do not reconcile with all the observations. In this region, the forebulge stress is either considered ocean-ward, responding to the Sumatran arc collapse[25], or trench-ward due to a locally-increased slab pull, up to ~3 times that of the Java slab[48], or also follows a localised increment of plate boundary velocity[57]. However, these models are at odd with the contraction in the arc, opposed to collapse, and cannot be accounted for in the one-sided slab pull models proposed.

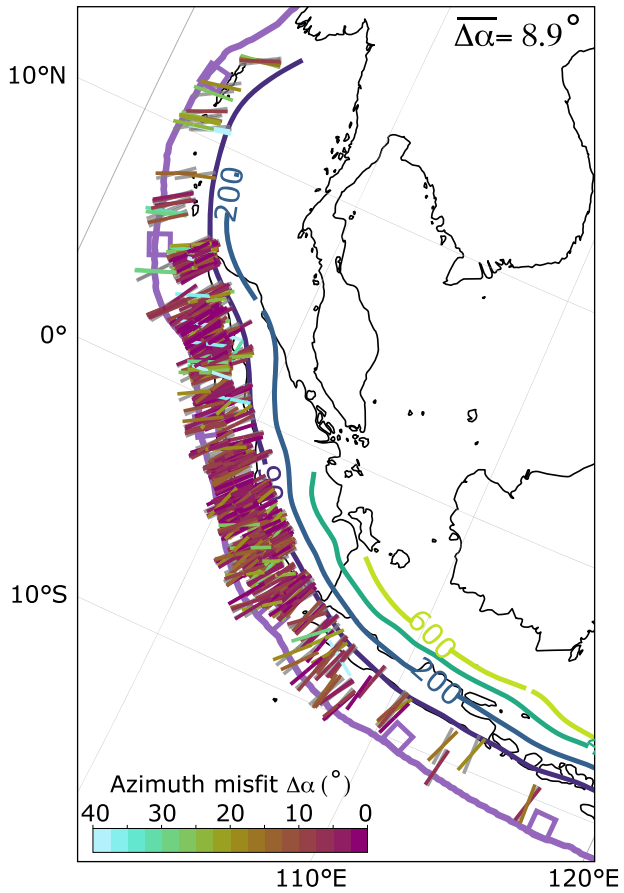

Fig. 6 | Modelled megathrust horizontal maximum compressive stress orientations and comparison with P-axes. *P*-axes from megathrust earthquakes in the 1964–2021 ISC-EHB catalogue[62]. Color indicates the azimuthal misfit (Δα) between the P-axis orientations and the modeled stress orientations along the megathrust; gray lines represent model-predicted stress directions. The mean misfit is shown in the upper right corner. All the panels were created with open-source software Python and library Matplotlib.

Stress and strength heterogeneities and the seismicity of the Sunda megathrust

The comparison between modelled and observed tectonics and current strain of the Sunda margin supports inferences on the long-term stresses acting on the plate interface and its strength, illustrating the potential role of subduction-driven deviatoric stresses. Therefore, we propose a comparison between computed stress and that inferred from observed megathrust seismicity.

The megathrust compressive stress in our models helps reconciling the enigmatic obliquity of convergence with trench-normal forearc compression and earthquakes' P-axes in Sunda. While our modelling does not simulate earthquakes directly, it constrains stress regimes that are comparable to those inferred by earthquakes inversions, through the relation of megathrust stresses and radiated and fracture energy and frictional dissipation. This approach leverages the well-established empirical relationship between stress drop and moment magnitude[59], while acknowledging that constraining the precise relationship between fracture energy and earthquake magnitude remains an open challenge[60].

The models reproduce both the trench-parallel and trench-perpendicular components of plate motions and the transcurrent regimes in the back-arc, while compression on the megathrust is perpendicular to the trench. This is illustrated in a comparison of the direction of model's compressive horizontal stress axes at the megathrust and the P-axes in the seismic catalogue (Fig. 6), which are near-perpendicular to the trench all along the Sunda margin[61]. Then, we compare the direction of the observed P-axes with the model's compressive stress directions interpolated at the location of the earthquakes and provide a measure of the azimuth misfit between the observation and the calculation (colour bar), Δα, as well as the model stress directions (grey). This comparison shows a consistent alignment between the models' compressive stress axes and the P-axes, with a mean azimuth misfit $\bar{\Delta\alpha}$ of only 8.9°. The misfit is larger in the northernmost Andaman sectors, ~20°, while only few individual events have misfits up to 40°.

We further illustrate the magnitude of the normal stresses on the megathrust and speculate on their potential role as seismic barriers. High normal stress on megathrusts can be associated with barriers to seismic rupture[2], if it increases the frictional strength in excess of the tectonic stresses loading the megathrust. In our models, the pattern and values of deviatoric normal stresses on the megathrust represent values sustained over long term, ~700 kyr. The main features of the stress pattern are reproduced by all the models (Supplementary Fig. S11), and we show the model with full Indian ocean plate and lower mantle constrained by tomography MITP08 (Model 3c, Fig. 7). Deviatoric normal stresses are consistently τ_n > ~40 MPa in the southern portion of the megathrust, whereas these decrease to lower values progressively, from northern Sumatra to Andaman (Fig. 7a). A projection on the Java-southern Sumatra interface (Fig. 7b), shows patches with τ_n consistently high from surface to depth of ~70 km. The projection of the model stress also shows the location of (megathrust-

https://doi.org/10.1038/s41467-025-65824-7

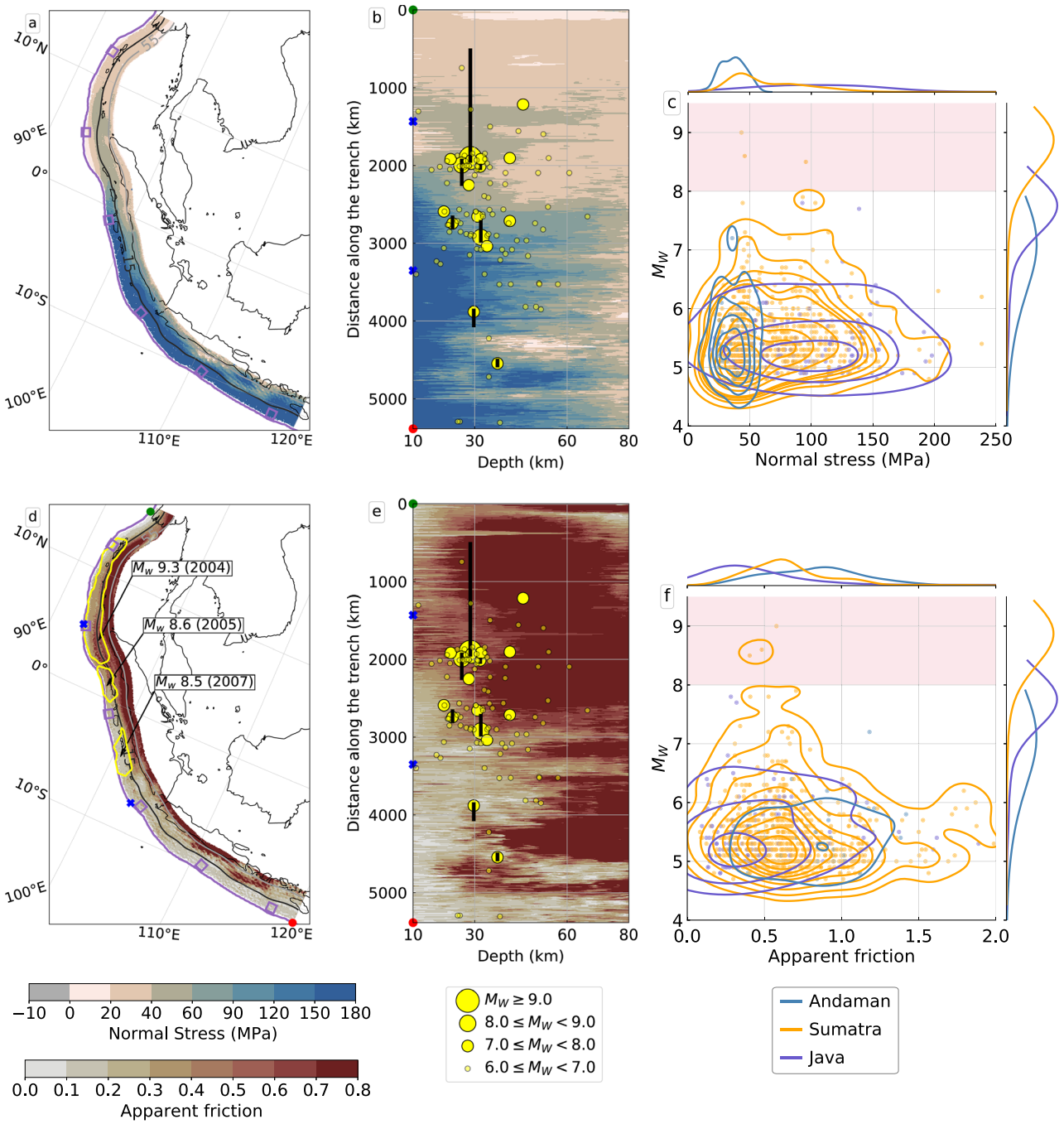

Fig. 7 | Modelled normal stress and apparent friction along the Sunda megathrust. a Map of the deviatoric normal stress (τ_n) on the megathrust in the Model 3c. The magenta line with squares marks the location of the trench. Contour lines represent variations in megathrust depth. b) Megathrust deviatoric normal stress (τ_n) projected in Cartesian space, overlaid with seismicity data from the 1964-2021 ISC-EHB catalogue[62], with available rupture lengths. **c** Plot of moment magnitude (M_w) versus normal stress (τ_n) for the earthquakes shown in (**b**). The τ_n values are sampled at the locations of the earthquakes. Probability density functions (pdfs) for the τ_n distribution are displayed at the top of the panel, while pdfs for the energy released (weighted magnitude) are shown on the side. **d** Map of the apparent friction (μ) on the megathrust in the Model 3c and rupture surface of the three highest energy earthquakes (yellow thick contours). **e** Apparent friction projected in Cartesian space, overlaid with seismicity data as in (**b**). **f** Plot of moment magnitude (M_w) versus apparent friction for the earthquakes shown in panel, as in (**c**). All the panels were created with open-source software Python and library Matplotlib.

only) earthquakes from the seismic catalog[62], with rupture length for the largest events (black bars).

Then, we propose a comparison between the magnitude of the stress released during earthquakes and that ideally loaded by subduction dynamics, modelled here. This comparison remains purely speculative, as we do not model the seismic rupture, yet relies on the empirical correlation between the seismic magnitude, linearly dependent on the stress released during earthquakes, and the cumulative moment, i.e., the total energy released over the interval of the catalogue. We sample the model stresses in the location of the seismic events and plot the values in a M_w vs. τ_n space (Fig. 7c), with probability density functions (pdf) for the model stresses (Fig. 7c, top horizontal) and the cumulative energy released for a given magnitude (Fig. 7c, lateral vertical axis). The pdfs illustrate both bivariate and univariate distributions, while the marginal kernel density estimations (KDE) plots along the axes represent the individual distributions across three

segments of the Southeast Asian subduction zone. Additionally, weights were assigned to M_w observations, so that the pdfs reflect the relative amount of energy released. The pdfs show consistent clustering of seismic events in patches where computed normal stress τ_n < ~ 50 MPa in Sumatra and Andaman. This segment is where the highest M_w and cumulative energy are recorded (pdfs on the vertical axis). Instead, in the Java segment, the energy released over the seismic catalogue is one order of magnitude lower and the model normal stresses in the Java segment are consistently larger, mostly clustered around 100 MPa.

The distribution of high modelled deviatoric normal stresses in the segment with lowest magnitude earthquakes and overall lowest seismic energy release, may support the inference on seismic barriers[63]. The Java segment is mostly aseismic, as of this writing, implying creeping conditions[64] in agreement with the invoked increased normal stress[63]. The normal stress on the megathrust seismogenic zone is unlikely to change significantly during the earthquake cycle, as megathrust earthquakes act primarily to release fault-parallel stored (elastic) shear stress. Fault regions with higher fracture energy can act as either high-energy asperities or barriers, depending on whether or not respectively the fault shear stress is increased by tectonic processes[65]. The high-energy asperity model typically requires shear stress concentration due to surrounding fault creep[2]. Such stress concentration is not applicable at the subduction margin scale, in which case a megathrust with broad regions of high fracture energy may host only small to moderate sized earthquakes where localised stress concentrations occur during the earthquake cycle. In fact, the Java segment has manifested episodic great earthquakes, such as the 2006 M_w 7.7, which may respond to higher normal stress[28], too, but at a scale where localised stress concentration can occur or else related to seamounts and sea-floor roughness[64].

We finally show the strength along the modelled megathrust (Fig. 6d), as apparent friction $\mu = \tau_s/\tau_n$, the ratio of shear to normal deviatoric stress[17], and speculate on the conditions for rupture the tectonics stress may induce. In our work, this is a long-term averaged effective strength and approaches the interseismic strength[14]. Most importantly, this ratio considers only the deviatoric stress components, due to the coupled slab-mantle system, and the shearing along the margin. This is net of lithostatic and pore pressure, therefore differs from the friction commonly calculated as the result of lithostatic pressure[17], where the shear-to-normal stress ratio is constrained only by static net load and thrust's dipping angle. Note that the averaged apparent friction is not necessarily the local frictional fault strength. This latter varies over the duration of the single seismic event due to shear stress release, while the normal stress is unlikely to change. However, considering the modest stress drop during earthquakes[66], the difference between the averaged and time-dependent friction remains minor. Friction may vary from the laboratory-constrained value of 0.65 to much lower, under the effect of pore pressure[17], therefore we focus on relative values along the megathrust. We saturate the scale in Fig. 7d and e at $\mu = 0.85$, considering that higher values fall above the yield strength envelope. For near lithostatic fluid pore pressure commonly assumed in fault zones, i.e., $\lambda = 0.95$, this values becomes equivalent to 0.0425 (see Methods).

The distribution of frictional strength in the models varies remarkably on the subduction interface and is highest at shallow depth along the northern portion of the megathrust. Lowest values, $0.08 < \mu < 0.4$ (0.0004 to 0.02, for $\lambda = 0.95$) characterise the shallowest portion of the Java–southern Sumatra, < ~55 km depth (Fig. 7d), while higher values are measured deeper. Following the previous discussion of a relatively higher normal stress acting on Java, we suggest that this would only translate to conditions for margin-scale ruptures if matched by elevated shear stress, manifesting as a high effective long-term margin strength. The modelled apparent friction instead supports our speculation that the region of increased normal stress acts as a frictional barrier at the margin scale, with low friction in southern Sumatra and Java at shallow depth, in agreement with the general observation of aseismic creep near the trench, offshore Sumatra, after the 2005 and 2007 earthquakes[64]. Similarly, friction increases at depth, along the Java subduction zone, yet exceeding the seismogenic depth, thus suggesting conditions for creeping. This is compatible with the inferred creep along this segment[64], as discussed above. The friction values progressively increase northward, with $\mu > 0.5$ (0.025 for $\lambda = 0.95$) over the whole northern Sumatra-Andaman segment, consistently high over most of the interface depth (Fig. 7d). The modelled friction reaches highest values also at shallow depths further north, reaching depth comparable to the 2004 and 2005 ruptures (Fig. 7d). The plot of the historical earthquakes catalogue on the mapping of apparent friction illustrates the clustered occurrence on this northern segment (Fig. 7e), whereas the statistical distribution shows that the largest occurrences are for values > 0.5 in Sumatra and Andaman, and consistently lower in Java (Fig. 7f). These correlate with the energy released, higher for the combined Sumatra-Andaman segments, where the probability density functions (pdf) are consistently clustered around $\mu > 0.5$, as opposed to Java, where lower energy released correlated with values of $\mu < 0.5$.

The models' friction is highest in northern Sumatra, then decreasing northwards in Andaman, and is compatible with the initial conditions for earthquake and slip propagation simulations during the 2004 Sumatra-Andaman earthquake and tsunami[67]. In the published work, the loading stress is due to the plate motions, comparable to the subduction-driven deviatoric stress shown here, whereas the static stress is limited to a very small fraction, to match the stress drop during a range of earthquakes, $O(10)$ MPa ref. 66, and keep major stress orientation sub-horizontal as observed in megathrust earthquakes[16]. The net pressure acting on megathrusts is usually obtained lowering the topographic pressure by a (arbitrary) high pore pressure[13,67,68]. Here, we have shown that the deviatoric normal stress is in the same order, < 40 MPa in the segments where great earthquakes cluster, although these magnitude and favorable horizontal orientation emerge self-consistently from the dynamics of subduction. Comparable normal stress and friction imply that the modelled shear stresses τ_s must compare to published values, too. Our deviatoric shear stress is clustered around 30-50 MPa in Sumatra (Supplementary Fig. S12), matching Sumatran values in the same range from static force balance[13], and slightly, yet expectedly, higher than values constrained by thermal modelling on this megathrust[15], ~20 MPa.

Limitations of this study and conclusions

The computational challenge associated with seismotectonics modelling imposes several simplifications. These result in limitations, but also offers an opportunity to test the simplifications for the benefit of computational modelling. While the assumptions help isolate fundamental mechanisms, they may also introduce limitations in capturing the full complexity of natural systems. This requires high spatial resolution in a broad modelling domain to simulate incremental deformation over million years, and prompted different strategies aimed to addressing the seismic cycles in two dimensions[10,35,69], expanded it to a 2.5-dimensional approach[36] or addressed long-term intra-slab stresses in three dimensional global models[38]. Here, we focused on a specific region to further constrain and validate the modelling simplifications. We found that the first-order stress field around subduction zones is captured by modelling only the upper mantle structures in three dimensions, including the mechanical slab depth, beneath the margin, assuming a Newtonian mantle, and limiting the solution of non-linearities to the plastic interface. Additional complexities, i.e., non-linearities in the mantle and far-field forces, e.g., ridge push, increase sensitively the computational cost, while the differences in the outcomes are minor and beyond what can be validated against the observables. This suggest that a reduced computational

three-dimensional space including mostly the upper mantle-slab interaction beneath the Sunda margin may be sufficient to capture the mechanisms at play. However, our modelling focuses on an average long-term behavior and does not capture the interactions leading to stress loading and release during the seismic cycles, for which complex rheologies, including elasticity, and megathrust non-linear constitutive laws, including fluids, may become fundamental.

The models also adopt many simplifications of the features of this area. The models embed what we found the most fundamental feature, the varying depth of the mechanical slab, yet, neglect other smaller scale features, such as the zone of low tectonic coupling on the Sumatra megathrust, around the equator, which may be associated to the subduction of the Investigator Fracture Zone[70]. Similarly, the dataset used for the slab geometry does include tear faults, which may contribute to the segmentation of seismicity along the southern Sumatran segment[53], however the rheological behavior of these discontinuities remains unconstrained, therefore we do not address their role further, here. Additionally, we do not consider internal structures and composition of the megathrust. These have a clear role in the nucleation of megaearthquakes, that is, on the strength, and may depend on seafloor roughness, sediments, seamounts, and curvature[8,64], which impact the asperities and the correlated high seismic coupling[70]. We excluded the subduction zones east of Banda assuming they only exert far-field forces, proven to have a negligible impact on margin stresses, here, although this remains to be fully investigated.

Finally, a note of caution regarding the use of the seismic catalogue in this study is in order. While these catalogues provide an invaluable record of earthquake occurrences, they are inherently limited by the temporal and spatial coverage of instrumental and historical observations, which may lead to incompleteness and biased assessments of long-term tectonic processes. The impact of incompleteness is here minimised using published analysis of seismic coupling[22] and its compatibility of the deformation across timescales[18] in this area, although cannot be excluded. Furthermore, long-term and transient seismic strain are not easily separated, which is here mitigated in the geodetically-constrained strain rate dataset, in which the proximity in time and space to major earthquakes has been removed[19]. These limitations invoke a careful interpretation of seismic data and underscore the importance of integrating datasets, as suggested here, to improve our understanding of underlying tectonics and dynamics, although this may remain speculative.

Stress generated by subduction dynamics is a primary driver of tectonics and destructive earthquakes along convergent margins, however the link between the seismotectonics of margins and the deep subducting lithosphere has continued to elude. We address the case of the Sunda margin, southeastern Asia, where the location of the highest seismic energy and intense tectonics deformation, in the northern Sumatra-Andaman, is at odd with the inferred weak tectonic forces of the shortest slab in the region. Using a high-performance computational approach, we reproduce the subduction of the Indo-Australian plate and the whole mantle underneath to explore the role subduction dynamics have on the seismotectonics of the highly-seismic Sunda margin. Our models reproduce the oblique plate convergence, the advancing trench motions and interseismic contraction in Sumatra, and reconcile with the trench-perpendicular compressional axes along the margin, aligned with the inferred earthquakes' P-axes. The Sumatran modelled features are due to an excess tectonic coupling, i.e., stress across the margin, as the result of the slab step beneath Sumatra, where the slab becomes abruptly shorter. The slab step result in excess forcing of the Java slab onto the northern margin and additional trench-ward tractions due to the fast mantle flow around the deep-subducting Java slab. The remarkable match between the simulations and the observed plate motions, tectonics and interseismic strain rates validates the models' force balance, providing insight into the stresses, that is, the actual long-term strength of the Sunda megathrust. Models' deviatoric stress magnitude and direction agree with published values of megathrust stress components and friction, constrained by observed stress drops during large earthquakes, and are in the same order of the inferred net static pressure on megathrusts. We show that large normal stresses in the south and larger strength in the north are compatible with the clustering of highest seismic energy released along the Sumatra-Andaman megathrust and the geodetically-constrained barriers in the southern segment. Although megathrust characteristics and their time-dependence are simplified, we show that the stress field of the whole Sunda margin is influenced by the lateral distribution of slab mass. The abrupt shortening of the slab beneath Sumatra generates excess forcing of the deep Java slab onto the neighbouring segments, where intense tectonics activity above a short, young slab may otherwise remain unexplained. In turn, this affects the long-term strength of megathrusts and sets conditions favourable for rupture and earthquake nucleation at the regional scale.

Methods

We model subduction in a regional spherical space as the Stokes flow of an incompressible fluid with infinite Prandtl number. Under these assumptions, the equations of conservation of mass and momentum reduce to:

$$\nabla \cdot \mathbf{u} = 0 \tag{1}$$

$$-\nabla p + \eta \nabla^2 \mathbf{u} + \rho \mathbf{g} = 0 \tag{2}$$

where $\mathbf{u}$ is the velocity vector, p the pressure, η the viscosity, and $\rho\mathbf{g}$ is the force owing to density variations and (downward) gravity acceleration, respectively. In the Supplementary Information we provide a derivation of the equation of momentum from the force balance of subduction. We neglect the energy conservation equation, as we solve for the instantaneous flow, which inhibits the effect of thermal diffusion. The continuity equations describing the Stokes flow in their non-dimensional form are solved using the particle-in-cell finite element code Underworld[71].

The stress tensor $\boldsymbol{\sigma}$ is defined as the sum of the isotropic and deviatoric components:

$$\boldsymbol{\sigma} = -\mathrm{p}\mathbf{I} + \boldsymbol{\sigma}' \tag{3}$$

where $\mathbf{I}$ and $\boldsymbol{\sigma}'$ are the identity tensor and the deviatoric stress, respectively.

The constitutive law relating the stresses and strain rates is given by the Newtonian creep of the form:

$$\boldsymbol{\sigma}' = 2\eta\dot{\boldsymbol{\varepsilon}} = \eta\left[\nabla\mathbf{u} + (\nabla\mathbf{u})^{\mathrm{T}}\right] \tag{4}$$

where $\dot{\boldsymbol{\varepsilon}}$ is the strain rate tensor.

The viscosity η is defined by constitutive law that embeds the creep and plastic flow. The creep law considers the effect of both diffusion and dislocation creep, that is, Newtonian and non-Newtonian creep:

$$\eta_{\mathrm{creep}} = \eta_0 \left(\frac{\dot{\varepsilon}_{\mathrm{II}}}{\dot{\varepsilon}_{\mathrm{T}}}\right)^{\frac{1-n}{n}} \tag{5}$$

where η_0 is the reference (Newtonian) viscosity, $\dot{\varepsilon}_{II}$ is the (square root of the) second invariant of the strain rate tensor, n is the power-law exponent and $\dot{\varepsilon}_{\mathrm{T}}$ is the transition strain rate, i.e., the value at which the dominant deformation mechanism switches from linear to non-linear creep, i.e., diffusion to dislocation creep. We have tested various

mantle creep laws from purely Newtonian, i.e., $n = 1$, to non-Newtonian, i.e., $n = 3$, and tested the role of different transition strain rates. The transition strain rate controls the area of linear vs. non-linear deformation. For lower values tested, the mantle is predominantly under non-Newtonian flow, accommodating stresses by dislocation creep. With increasing values of $\dot{\varepsilon}_T$, the distribution of dislocation creep flow reduces to high stresses areas in the mantle, whereas the rest is under diffusion creep (Supplementary Fig. S3c). Laboratory and geodynamics constraints suggest $\dot{\varepsilon}_T \sim 10^{-15}$ s^{-1}, in agreement with seismic evidence of a mantle predominantly deforming under diffusion creep[72].

Plasticity is implemented in the models using a yielding criterion:

$$\tau_y = C0 + \mu p(1-\lambda), \text{ at } \tau > \tau_y \quad (6)$$

where C_0 is the cohesion and μ the friction at which yielding set forth in the viscous material and λ is the pore pressure fraction. To fit the common assumption of near-lithostatic pore pressure, λ is set to 1, and the yield stress reduces to:

$$\tau_y = C_0 \quad (7)$$

The models assimilate the yielding criterion through a composite viscoplastic effective viscosity:

$$\eta = \min\left(\eta_{\text{creep}}, \frac{\tau_y}{2\dot{\varepsilon}_{II}}\right) \quad (8)$$

where $\dot{\varepsilon}_{II}$ is the second invariant of strain rate tensor.

We have simulated the geodynamics of the Southeast Asian subduction zone in a part of a spherical shell. The model domain is discretised using a uniformly spaced mesh in the longitude and latitude direction and a non-uniformly spaced mesh in the radial direction. As a result, the element size is $15 \times 15 \times 10$ km in the upper mantle and $15 \times 15 \times 37$ km in the lower mantle in longitude, latitude, and radial direction. We embed in each element 20 Lagrangian particles, capitalizing on the code's ability to track material properties and increase the resolution, allowing a more accurate recovery of different materials stress. All boundaries are set to free slip conditions. For full details on each model setup, refer to Supplementary Tables S1 and S2.

We treat the Indo-Australian subducting plate as a single plate. We rotate the boundary box of the numerical model by 16° clockwise to avoid the implementation of viscosity weakness along the Owen Fracture Zone (OFZ). The rotation angle is calculated by optimizing the angle between the boundary box and velocities of the Indo-Australian plate in the NNR reference frame (Supplementary Table S3). The slab geometry in the upper mantle, that is, the subducted lithosphere, is reconstructed using slab depth and thickness provided by the Slab2 dataset[27]. The thickness h of the oceanic plate, that is, the unsubducted lithosphere, is recovered using the half-space cooling model, defined by the 1300 °C isotherm, and oceanic crustal ages dataset[41] as $h = 2.32\sqrt{\kappa t}$, where $\kappa = 10^{-6}$ m^2 s^{-1} and age t in s, for $t \leq 100$ Ma, and $h = 130$ km for older lithosphere. The lithospheric thickness is chosen to match the thickness from the dataset Slab2. This includes thinning around the Capricorn zone, Wharton Basin, however we do not address the putative deformation zone between Indian, Capricorn and Australian plates, to avoid the implementation of ill-posed viscosity weaknesses. The density contrast with the underlying mantle is 50 kg m^{-3} (refs. 30,73). The continental lithosphere is thinned to 90 km, implying a buoyancy increase of ~30%, while in Model 3c we additionally vary the density of the Indian slab (see Supplementary Table S2). The upper plate is modelled as a uniform lithosphere, with no internal boundaries and constant thickness of 90 km. The lower mantle density anomalies are scaled from the tomographic models using scaling factor of 0.3 and 0.6 for the S-wave and P-wave tomographies to convert velocity anomalies into density anomalies, respectively, while in the upper mantle we ignore density anomalies from tomographies due to their poor resolution, following ref.[45]. The viscosity in the mantle varies only in the radial direction, we set a viscosity jump of a factor 30 between the upper and lower mantle.

The subducting lithosphere has a viscoplastic rheology in the top 30 km and adopt a linear viscous flow law in the rest of the slab. In the models, the brittle ductile transition is defined self-consistently, i.e., occurs at shallower depths, according to the coupling stress. The choice of the maximum viscoplastic layer is based on the observed maximum depth of the brittle to ductile transition in an oceanic plate[74]. The viscoplastic rheology decouples effectively the subducting and upper plate and has been tested against stress at subduction zones, tectonics and earthquakes simulations[34,35,40,75]. For simplicity, the upper plate is treated as a uniform-thickness viscous plate to highlight the role of boundary stresses, as opposed to those resulting from geometrical singularities arising from upper plate structures.

Tests of viscosity, cohesion and numerical resolution, among others, are performed in a range of different models in Cartesian and spherical coordinates systems and two- and three-dimensional spaces, to reduce the computational cost and are publicly available[76].

Data availability

The rupture surfaces data are available at http://equake-rc.info/srcmod/, seismic catalogue International Seismological Centre (2024), On-line Event Bibliography, https://doi.org/10.31905/EJ3B5LV6.

Code availability

The code Underworld2 version 2.8.1b is available via Zenodo at https://doi.org/10.5281/zenodo.3384283.

References

1. Bilek, S. L. & Lay, T. Subduction zone megathrust earthquakes. *Geosphere* **14**, 1468–1500 (2018).
2. Avouac, J.-P. From geodetic imaging of seismic and aseismic fault slip to dynamic modeling of the seismic cycle. *Ann. Rev., Earth Plan. Sci.* **43**, 233–271 (2015).
3. Wang, K., Hu, Y. & He, J. Deformation cycles of subduction earthquakes in a viscoelastic Earth. *Nature* **484**, 327–332 (2012).
4. Wang, K. & Dixon, T. "Coupling" semantics and science in earthquake research. *Eos, Trans. Am. Geophys. Union* **85**, 180 (2004).
5. Nishikawa, T. & Ide, S. Earthquake size distribution in subduction zones linked to slab buoyancy. *Nat. Geosci.* **7**, 904–908 (2014).
6. Heuret, A., Conrad, C. P., Funiciello, F., Lallemand, S. & Sandri, L. Relation between subduction megathrust earthquakes, trench sediment thickness and upper plate strain. *Geophys. Res. Lett.* https://doi.org/10.1029/2011GL050712 (2012).
7. Conrad, C. P., Bilek, S. & Lithgow-Bertelloni, C. Great earthquakes and slab pull: interaction between seismic coupling and plate-slab coupling. *Earth Plan. Sci. Let.* **218**, 109–122 (2004).
8. Bletery, Q. et al. Mega-earthquakes rupture flat megathrusts. *Science* **354**, 1027–1031 (2016).
9. van Rijsingen, E. et al. How subduction interface roughness influences the occurrence of large interplate earthquakes. *Geochem. Geophys. Geosys.* **19**, 2342–2370 (2018).
10. Brizzi, S., van Zelst, I., Funiciello, F., Corbi, F. & van Dinther, Y. How sediment thickness influences subduction dynamics and seismicity. *J. Geophys. Res. - S.E.* **125**, e2019JB018964 (2020).
11. Stein, S., Geller, R. J. & Liu, M. Why earthquake hazard maps often fail and what to do about it. *Tectonophys* **562**, 1–25 (2012).
12. McCaffrey, R. Global frequency of magnitude 9 earthquakes. *Geology* **36**, 263–266 (2008).

13. Dielforder, A., Hetzel, R. & Oncken, O. Megathrust shear force controls mountain height at convergent plate margins. *Nature* **582**, 225–229 (2020).
14. Wang, K. & Hu, Y. Accretionary prisms in subduction earthquake cycles: the theory of dynamic Coulomb wedge. *J. Geophys. Res. - S.E.* https://doi.org/10.1029/2005JB004094 (2006).
15. England, P. On shear stresses, temperatures, and the maximum magnitudes of earthquakes at convergent plate boundaries. *J. Geophys. Res. - S. E.* **123**, 7165–7202 (2018).
16. Hardebeck, J. L. Stress orientations in subduction zones and the strength of subduction megathrust faults. *Science* **349**, 1213–1216 (2015).
17. Scholz, C. H. Earthquakes and friction laws. *Nature* **391**, 37–42 (1998).
18. Zuhair, M., Gollapalli, T., Capitanio, F. A., Betts, P. G. & Graciosa, J. C. The role of slab steps on tectonic loading along subduction zones: inferences on the seismotectonics of the Sunda convergent margin. *Tectonics* **41**, e2022TC007242 (2022).
19. Kreemer, C., Blewitt, G. & Klein, E. C. A geodetic plate motion and global strain rate model. *Geochem. Geophys. Geosys.* **15**, 3849–3889 (2014).
20. Ishii, M., Shearer, P. M., Houston, H. & Vidale, J. E. Extent, duration and speed of the 2004 Sumatra–Andaman earthquake imaged by the Hi-Net array. *Nature* **435**, 933–936 (2005).
21. McCaffrey, R. The tectonic framework of the Sumatran subduction zone. *Ann. Rev. Earth Plan, Sci.* **37**, 345–366 (2009).
22. Scholz, C. H. & Campos, J. The seismic coupling of subduction zones revisited. *J. Geophys. Res. - S.E.* https://doi.org/10.1029/2011JB009003 (2012).
23. Schellart, W. P. Subduction zone trench migration: Slab driven or overriding-plate-driven? *Phys. Earth Plan. Int.* **170**, 73–88 (2008).
24. Raghuram, G., Capitanio, F. A. & Radhakrishna, M. Flexural analysis along the Sunda trench: bending, buckling and plate coupling. *Tectonics* **37**, 3524–3544 (2018).
25. Craig, T. J. & Copley, A. Forearc collapse, plate flexure, and seismicity within the downgoing plate along the Sunda Arc west of Sumatra. *Earth Plan. Sci. Lett.* **484**, 81–91 (2018).
26. Sieh, K. & Natawidjaja, D. Neotectonics of the Sumatran fault, Indonesia. *J. Geophys. Res. - S. E.* **105**, 28295–28326 (2000).
27. Hayes, G. P. et al. Slab2, a comprehensive subduction zone geometry model. *Science*, **362**, 6410(2018).
28. Hutchings, S. J. & Mooney, W. D. The seismicity of Indonesia and tectonic implications. *Geochem. Geophys. Geosys.* **22**, e2021GC009812 (2021).
29. Radhakrishna, M., Lasitha, S. & Mukhopadhyay, M. Seismicity, gravity anomalies and lithospheric structure of the Andaman arc, NE Indian Ocean. *Tectonophysics* **460**, 248–262 (2008).
30. Ghose, R., Yoshioka, S. & Oike, K. Three-dimensional numerical simulation of the subduction dynamics in the Sunda arc region, Southeast Asia. *Tectonophys* **181**, 223–255 (1900).
31. Zahirovic, S., Seton, M. & Müller, R. D. The Cretaceous and Cenozoic tectonic evolution of Southeast Asia. *Solid Earth* **5**, 227–273 (2014).
32. Graciosa, J. C. et al. Testing driving mechanisms of megathrust seismicity with explainable artificial intelligence. *J. Geophys. Res.* **130**, e2024JB028774 (2025).
33. Van Zelst, I., Wollherr, S., Gabriel, A.-A., Madden, E. H. & van Dinther, Y. Modeling megathrust earthquakes across scales: One-way coupling from geodynamics and seismic cycles to dynamic rupture. *J. Geophys. Res. - S. E.* **124**, 11414–11446 (2019).
34. Beall, A., Fagereng, Å., Davies, J. H., Garel, F. & Davies, D. R. Influence of subduction zone dynamics on interface shear stress and potential relationship with seismogenic behavior. *Geochem. Geophys. Geosys.* **22**, e2020GC009267 (2021).
35. Sobolev, S. V. & Muldashev, I. A. Modeling seismic cycles of great megathrust earthquakes across the scales with focus at post-seismic phase. *Geochem. Geophys. Geosys.* **18**, 4387–4408 (2017).
36. Fang, J., Gurnis, M. & Lapusta, N. Dynamic emergence of plate motions and great megathrust earthquakes across length and time scales. *Geophys. Res. Lett.* **51**, e2024GL110821 (2024).
37. Billen, M. I. Deep slab seismicity limited by rate of deformation in the transition zone. *Sci. Adv.* **6**, eaaz7692 (2020).
38. Stadler, G. et al. The Dynamics of Plate Tectonics and Mantle Flow: From Local to Global Scales. *Science* **329**, 1033–1038 (2010).
39. Becker, T. W. & Faccenna, C. Mantle conveyor beneath the Tethyan collisional belt. *Earth Plan. Sci. Lett.* **310**, 453–461 (2011).
40. Capitanio, F. A., Faccenna, C., Zlotnik, S. & Stegman, D. R. Subduction dynamics and the origin of Andean orogeny and Bolivian Orocline. *Nature* **480**, 83–86 (2011).
41. Müller, R. D., Sdrolias, M., Gaina, C. & Roest, W. R. Age, spreading rates, and spreading asymmetry of the world's ocean crust. *Geoc. Geophy. Geosys.* **9**, Q04006 (2008).
42. Li, C., van der Hilst, R. D., Engdahl, E. R. & Burdick, S. A new global model for P wave speed variations in Earth's mantle. *Geochem. Geophys. Geosys.* https://doi.org/10.1029/2007GC001806 (2008).
43. Becker, T. W. & Boschi, L. A comparison of tomographic and geodynamic mantle models. *Geochem. Geophys. Geosys.* **3**, 415–432 (2002).
44. Rawlinson, N. & Spakman, W. On the use of sensitivity tests in seismic tomography. *Geophys. J. Int.* **205**, 1221–1243 (2016).
45. Steinberger, B. & Holme, R. Mantle flow models with core-mantle boundary constraints and chemical heterogeneities in the lowermost mantle. *J. Geophys. Res. - S.E.* https://doi.org/10.1029/2007JB005080 (2008).
46. Capitanio, F. A., Morra, G., Goes, S., Weinberg, R. F. & Moresi, L. India–Asia convergence driven by the subduction of the Greater Indian continent. *Nat. Geosci.* **3**, 136–139 (2010).
47. Goes, S., Capitanio, F. A. & Morra, G. Evidence of lower mantle slab penetration phases in plate motions. *Nature* **451**, 981–984 (2008).
48. Sandiford, M., Coblentz, D. & Schellart, W. P. Evaluating slab-plate coupling in the Indo-Australian plate. *Geology* **33**, 113–116 (2005).
49. Crameri, F., Tackley, P. J., Meilick, I., Gerya, T. V. & Kaus, B. J. P. A free plate surface and weak oceanic crust produce single-sided subduction on Earth. *Geophys. Res. Lett.* https://doi.org/10.1029/2011GL050046 (2012).
50. Kong, F., Gao, S. S., Liu, K. H., Zhang, J. & Li, J. Seismic anisotropy and mantle flow in the Sumatra subduction zone constrained by shear wave splitting and receiver function analyses. *Geochem. Geophys. Geosys.* **21**, e2019GC008766 (2020).
51. Becker, T. W., Schaeffer, A. J., Lebedev, S. & Conrad, C. P. Toward a generalized plate motion reference frame. *Geophys. Res. Lett.* **42**, 3188–3196 (2015).
52. Becker, T. W. & O'Connell, R. J. Predicting plate velocities with mantle circulation models *Geoc. Geophy. Geosys.* **2**, 2001GC000171 (2001).
53. Grevemeyer, I. & Tiwari, V. M. Overriding plate controls spatial distribution of megathrust earthquakes in the Sunda–Andaman subduction zone. *Earth Plan. Sci. Lett.* **251**, 199–208 (2006).
54. Widiyantoro, S., Supendi, P. & Rawlinson, N. A note on the seismicity of Sumatra, western Sunda Arc, Indonesia, in relation to the potential for back-arc thrusting. *Sci. Rep.* https://doi.org/10.1038/s41598-024-64076-7 (2024).
55. Koulali, A. et al. The kinematics of crustal deformation in Java from GPS observations: Implications for fault slip partitioning. *Earth Plan, Sci., Lett.* **458**, 69–79 (2017).
56. Martinod, J. & Molnar, P. Lithospheric folding in the Indian Ocean and the rheology of the oceanic plate. *Bull. de. la Soci.été Géologique de. Fr.* **166**, 813–821 (1995).

57. Gordon, R. G. & Houseman, G. A. Deformation of Indian Ocean lithosphere: Evidence for a highly nonlinear rheological law. *J. Geophys. Res. - S. E.* **120**, 4434–4449 (2015).
58. Warners-Ruckstuhl, K. N., Govers, R. & Wortel, R. Lithosphere–mantle coupling and the dynamics of the Eurasian Plate. *Geophys. J. Int.* **189**, 1253–1276 (2012).
59. Kanamori, H. The energy release in great earthquakes. *J. Geophys. Res.* **82**, 2981–2987 (1977).
60. Kammer, D. S. et al. Earthquake energy dissipation in a fracture mechanics framework. *Nat. Comm.* **15**, 4736–4740 (2024).
61. Heidbach, O. et al. The World Stress Map database release 2016: crustal stress pattern across scales. *Tectonophysics* **744**, 484–498 (2018).
62. Di Giacomo, D. et al. A new ISC service: the bibliography of seismic events. *Seismol. Res. Lett.* **85**, 354–360 (2014).
63. Molina-Ormazabal, D., Ampuero, J.-P. & Tassara, A. Diverse slip behaviour of velocity-weakening fault barriers. *Nat. Geosci.* **16**, 1200–1207 (2023).
64. Wang, K. & Bilek, S. L. Fault creep caused by subduction of rough seafloor relief. *Tectonophys.* **610**, https://doi.org/10.1016/j.tecto.2013.11.024 (2014).
65. Aki, K. Characterization of barriers on an earthquake fault. *J. Geophys. Res. - S. E* **84**, 6140–6148 (1979).
66. Allmann, B. P. & Shearer, P. M. Global variations of stress drop for moderate to large earthquakes. *J. Geophys. Res. - S.E.* **114**, https://doi.org/10.1029/2008JB005821 (2009).
67. Ulrich, T., Gabriel, A.-A. & Madden, E. H. Stress, rigidity and sediment strength control megathrust earthquake and tsunami dynamics. *Nat. Geosci.* **15**, 67–73 (2022).
68. Lamb, S. Shear stresses on megathrusts: Implications for mountain building behind subduction zones *J. Geophys. Res.* https://doi.org/10.1029/2005JB003916 (2006).
69. Dal Zilio, L., Van Dinther, Y., Gerya, T. V. & Pranger, C. C. Seismic behaviour of mountain belts controlled by plate convergence rate. *Earth Plan. Sci. Lett.* **482**, 81–92 (2018).
70. Chlieh, M., Avouac, J. P., Sieh, K., Natawidjaja, D. H. & Galetzka, J. Heterogeneous coupling of the Sumatran megathrust constrained by geodetic and paleogeodetic measurements. *J. Geophys. Res. - S.E.* https://doi.org/10.1029/2007JB004981 (2008).
71. Mansour, J. et al. Underworld2: Python geodynamics modelling for desktop, HPC and cloud. *J. Open Source Softw.* **5**, 1797–1799 (2020).
72. Billen, M. I. Modeling the Dynamics of Subducting Slabs. *Annu. Rev. Earth Planet. Sci.* **36**, 325–356 (2008).
73. Afonso, J. C., Ranalli, G. & Fernandez, M. Density structure and buoyancy of the oceanic lithosphere revisited. *Geophys. Res. Lett.* **34**, L10302 (2007).
74. Jackson, J., McKenzie, D. A. N., Priestley, K. & Emmerson, B. New views on the structure and rheology of the lithosphere. *J. Geol. Soc.* **162**, 453–465 (2008).
75. Capitanio, F. A., Stegman, D. R., Moresi, L. & Sharples, W. Upper plate controls on deep subduction, trench migrations and deformations at convergent margins. *Tectonophys* **483**, 80–92 (2010).
76. Gollapalli, T. et al. *Unravelling Tectonic Coupling And Loading Along The Sunda Margin Through 3-D Regional Numerical Modelling*, Monash University, (2022).

Acknowledgements

We acknowledge the provision of resources and services from the *National Computational Infrastructure* (NCI) and the support of *AuScope* and the Australian Government via the *National Collaborative Research Infrastructure Strategy* (NCRIS). Figures colormaps after Crameri, F. (2018). Scientific colour maps. Zenodo. https://doi.org/10.5281/zenodo.1243862.

Author contributions

Conceptualization: T.G., F.A.C. Methodology: T.G., F.A.C. Data processing: T.G. Writing: F.A.C. and T.G. led the writing with input from M.R., J.C.G., M.Z., A.B., L.D.Z.

Competing interests

The authors declare no competing interests.

Additional information

Supplementary information The online version contains supplementary material available at https://doi.org/10.1038/s41467-025-65824-7.

Correspondence and requests for materials should be addressed to Fabio A. Capitanio.

Peer review information *Nature Communications* thanks Serge Lallemand, Fabio Cramer and the other, anonymous, reviewer(s) for their contribution to the peer review of this work. A peer review file is available.